Soft Matter

PAPER

View Article Online
View Journal | View Issue

Cite this: *Soft Matter*, 2018, **14**, 5294

Size-dependence of the flow threshold in dense granular materials

Daren Liu and David L. Henann *

Received 24th April 2018,
Accepted 4th June 2018

DOI: 10.1039/c8sm00843d

rsc.li/soft-matter-journal

The flow threshold in dense granular materials is typically modeled by local, stress-based criteria. However, grain-scale cooperativity leads to size effects that cannot be captured with local conditions. In a widely studied example, flows of thin layers of grains down an inclined surface exhibit a size effect whereby thinner layers require more tilt to flow. In this paper, we consider the question of whether the size-dependence of the flow threshold observed in inclined plane flow is configurationally general. Specifically, we consider three different examples of inhomogeneous flow – planar shear flow with gravity, annular shear flow, and vertical chute flow – using two-dimensional discrete-element method calculations and show that the flow threshold is indeed size-dependent in these flow configurations, displaying additional strengthening as the system size is reduced. We then show that the nonlocal granular fluidity model – a nonlocal continuum model for dense granular flow – is capable of quantitatively capturing the observed size-dependent strengthening in all three flow configurations.

1 Introduction

A rheology for dense granular flows, relating the stress state to the shear strain-rate, may be extracted from homogeneous, planar shear flow data.[1,2] For example, consider a two-dimensional, quasi-monodisperse, dense granular system composed of dry, stiff, frictional disks with average disk diameter d and grain-material area-density ρ_s, so that the characteristic grain mass is $m = \rho_s \pi d^2/4$. The inertial rheology then relates the stress state – specifically, the pressure P and the shear stress τ (both with units of force per length in two-dimensional settings) – to the consequent shear strain-rate $\dot{\gamma}$. The aforementioned quantities may be expressed through the dimensionless groups $I = \dot{\gamma}\sqrt{m/P}$ and $\mu = \tau/P$, where I is referred to as the inertial number – representing the ratio of the microscopic time-scale associated with particle motion $\sqrt{m/P}$ to the macroscopic time-scale of applied deformation $1/\dot{\gamma}$ – and μ is the stress ratio. The inertial rheology then relates I and μ through a one-to-one functional relationship $\mu = \mu_{loc}(I)$, which is empirically fit. A common feature among different functional forms of the inertial rheology is a static yield value of the stress ratio – $\mu_{loc}(I \to 0) = \mu_s$. Consequently, the inertial rheology possesses a flow threshold in which steady flow is not possible when $\mu < \mu_s$ but steady flow becomes possible whenever μ exceeds μ_s.†

A logical next step is to apply this flow threshold to more complex flow configurations. A dense granular flow configuration that is more complex than homogeneous, planar shear – but still quite simple – is flow down a rough inclined surface. In inclined plane flow, the ratio of the shear stress to the pressure is a constant value at every point in the granular layer – as in planar shear – and is given through the inclination angle θ by $\mu = \tan\theta$. Therefore, the flow threshold associated with the inertial rheology predicts that flowing and non-flowing states are separated by a thickness-independent angle of repose $\theta_r = \tan^{-1}\mu_s$. However, extensive experiments and discrete-element method (DEM) simulations have shown that this is not the case.[1,6–10] Instead, thin granular layers do not flow for a range of θ greater than θ_r with additional strengthening as the layer thickness is decreased.

The inability of the inertial rheology to capture this size effect stems from its local nature – local in the sense that it relates the stress state to the strain-rate at a point. The size-dependence of the flow threshold in inclined plane flow arises due to nonlocal, cooperative effects at the microscopic grain level, which are not accounted for in the inertial rheology. In a thin granular layer, the proximity of the grains to the fixed, rough, inclined surface imbues the granular layer with additional strength. The converse manifestation of cooperativity may also be observed. Flow in one region of a granular medium can induce flow in far-away regions – even when these regions experience stress states that are beneath the flow threshold extracted from homogeneous, planar shearing. For example, in steady, non-uniform flows – such as annular shear,[11,12] split-bottom flow,[13] or gravity-driven heap flow[14] – a decaying flow field is observed, whereas the stress-based flow threshold of the inertial rheology would predict a sharp flow

School of Engineering, Brown University, Providence, RI, USA.
E-mail: david_henann@brown.edu

† In the common generalization of the inertial rheology to three-dimensions,[3,4] the flow threshold takes the form of a Drucker–Prager yield condition.[5]

cutoff. An additional example of this effect is the "secondary rheology" of intruders, whereby the motion of a boundary removes the flow threshold of the material everywhere, permitting far-away loaded objects to creep through the grains when otherwise they would remain static.[15]

While the effect of cooperativity on steady flow fields has been investigated in a diverse set of geometric configurations, studies exploring the size-dependence of the flow threshold in dense granular materials have been limited to inclined plane flow. To better elucidate the role of the stress field, the first purpose of this paper is to systematically explore the size-dependence of the flow threshold in different flow configurations with more complex stress fields. Specifically, we consider dense two-dimensional flows of stiff, frictional disks using DEM simulations in three flow configurations: (1) planar shear flow with gravity, (2) annular shear flow, and (3) vertical chute flow, and show that additional strengthening is observed as the system size is reduced in all three cases.

The second purpose of this paper is to rationalize the dependence of the flow threshold on the system size in the presence of different stress fields with a continuum model. A number of nonlocal continuum constitutive theories have been proposed, which are aimed at capturing various cooperative effects.[16–23] Among these, several have been applied to the flow threshold in inclined plane flow, such as integral equations representing a self-activated process;[16] Ginzberg–Landau theories based on a partial-fluidization order parameter,[17] the granular fluidity,[24] or the inertial number;[20] and extensions of kinetic theory.[23] In particular, our recent work[24] has shown that the nonlocal granular fluidity (NGF) model is capable of capturing the size-dependence of the flow threshold in inclined plane flows of glass beads. In this paper, we utilize the NGF model to obtain predictions of the size-dependence of the flow threshold in planar shear flow with gravity, annular shear flow, and vertical chute flow. Specifically, in each case, we calculate the analytical flow threshold predicted by the NGF model. Importantly, we show that the NGF model is capable of quantitatively describing the observed size-dependent strengthening in all three flow configurations, while simultaneously capturing steady flow fields.

The remainder of this paper is organized as follows. In Section 2, we discuss the specifics of our two-dimensional DEM simulations and verify our simulations against existing DEM data for stiff, frictional disks in planar shear flow from the literature.[2,25] In Section 3, we discuss the NGF model and its attendant description of the flow threshold. Then, in Section 4, we present the results of our DEM simulations in planar shear flow with gravity, annular shear flow, and vertical chute flow along with the predictions of the NGF model, comparing predictions of both the size-dependent flow threshold and steady flow fields to DEM data. We close with discussion and concluding remarks in Section 5.

2 Discrete-element method simulations

In this section, we provide details of our two-dimensional DEM methodology and briefly describe simulations of planar shear flow in order to verify our simulations against existing literature data.[2,25]

2.1 Simulated granular system

Following several previous works,[2,11,18,25] we consider a simulated, two-dimensional granular system consisting of a dense collection of circular disks. As in Section 1, the average disk diameter and the grain-material area-density are denoted as d and ρ_s, respectively, so that we may define a characteristic grain mass as $m = \rho_s \pi d^2/4$. The distribution of disk diameters involves a polydispersity of $\pm 20\%$ to prevent crystallization. We utilize a standard DEM grain interaction model.[2] Specifically, there is no force between non-overlapping grains, but when two grains overlap, they interact through a spring/dashpot contact law that accounts for elasticity, damping, and sliding friction. With $\delta_n \geq 0$ and δ_t denoting the normal and tangential components of the contact displacement, the normal contact force F_n is given linearly through the normal contact displacement with stiffness k_n and the relative normal velocity with damping coefficient g_n, *i.e.*, $F_n = k_n\delta_n + g_n\dot{\delta}_n$. The normal damping coefficient is specified through the coefficient of restitution for binary collisions e by $g_n = \sqrt{mk_n}(-2\ln e)/\sqrt{2(\pi^2 + \ln^2 e)}$. Tangential interactions are described by a stiffness k_t and damping coefficient g_t, which we take to be zero, so that the tangential contact force is $F_t = k_t\delta_t$. Importantly, the tangential contact force is limited by Coulomb friction, described by the inter-particle sliding friction coefficient μ_{surf}. Therefore, grain interactions are fully described through the parameter set $\{k_n, k_t, e, \mu_{surf}\}$. In order to simulate stiff, quasi-rigid grains, the normal stiffness is taken to be sufficiently large throughout, *i.e.*, $k_n/P > 10^4$, where P is the characteristic confining pressure for a given flow configuration. Next, it is well-appreciated that the precise values of k_t/k_n and e have a negligible impact on the phenomenology of dense flows of stiff disks,[2] and as in previous works,[11] we take $k_t/k_n = 1/2$ and $e = 0.1$. Finally, among the interaction parameters, μ_{surf} plays the most important role.[25] Exploring the effect of μ_{surf} on the flow threshold is beyond the scope of the present work, so we restrict attention to the case of $\mu_{surf} = 0.4$. The equations of motion for each particle are solved using standard molecular dynamics techniques using the open-source software LAMMPS.[26] For the most part, we restrict the time step to be 0.01 of the binary collision time, $\tau_c = \sqrt{m(\pi^2 + \ln^2 e)/4k_n}$, to ensure stable, accurate simulation results.‡

2.2 Planar shear flow

First, we perform simulations of planar shear flow in order to verify our DEM results against existing data reported in the literature. We consider a configuration consisting of a rectangular region of length $L = 60d$ in the x-direction and height $H = 60d$ in the z-direction that is filled with a dense collection of 3806 flowing grains and subjected to shearing through the relative motion of two parallel, rough walls, as shown in Fig. 1(a). The dense

‡ A larger time step is used for certain DEM simulations of planar shear flow and planar shear flow with gravity to save computation time. The time step is never taken to be greater than 0.1 of τ_c and has been verified to not affect results.

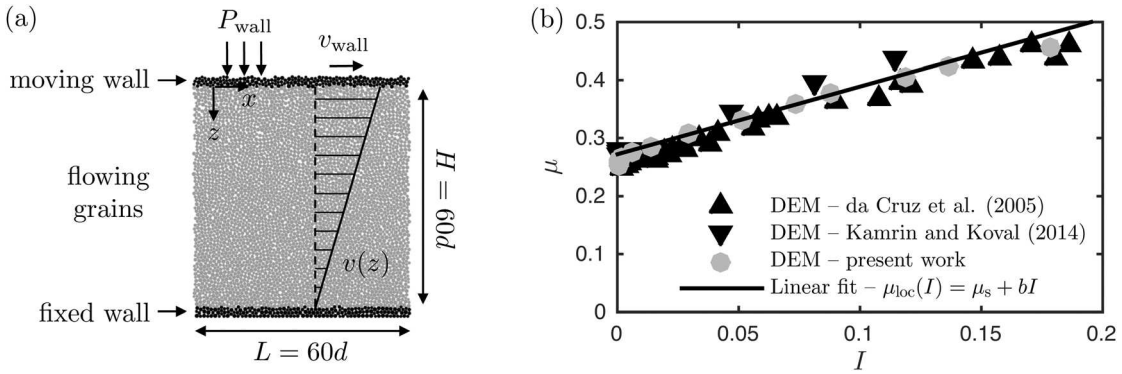

Fig. 1 (a) Configuration for two-dimensional DEM simulations of planar shear flow. Black grains denote rough walls, and gray grains denote flowing grains. (b) The local inertial rheology – μ *versus* I – for frictional disks with inter-particle sliding friction coefficient of $\mu_{\text{surf}} = 0.4$. Black symbols denote the DEM data of da Cruz *et al.*[2] and Kamrin and Koval,[25] and gray symbols denote the DEM data of the present work. The solid line denotes the fit of (1) with $\mu_s = 0.272$ and $b = 1.168$.

granular system is generated by allowing grains to sediment under the action of gravity, but gravity is absent in subsequent simulations of planar shear. Each of the two rough walls on top and bottom consists of a thin layer of touching glued grains, which are denoted as black in Fig. 1(a), while the flowing grains between the walls are denoted as gray. Regarding wall conditions, the bottom wall is fixed, and the velocity of the top wall in the x-direction is specified to be v_{wall}. Following da Cruz *et al.*[2] and subsequent works,[11,25] the velocity of the top wall in the z-direction is not zero – *i.e.*, H is not fixed. Instead, in order to maintain a target wall normal stress of $\sigma_{zz}(z = 0) = -P_{\text{wall}}$, the vertical position of the wall is continuously adjusted so that the value of H evolves through $\dot{H} = (-\sigma_{zz}(z = 0) - P_{\text{wall}})L/g_p$, where g_p is a damping parameter for vertical wall motion. Throughout, we take $g_p = 100\sqrt{mk_n}$. Periodic boundary conditions are utilized in the x-direction.

Next, we extract steady velocity and stress fields from DEM simulations of planar shear flow for a range of wall velocities, v_{wall}, and fixed wall pressure, P_{wall}. To ensure that steady flow is achieved, each simulation of planar shear is first run to a top-wall shear displacement of at least $400H$.§ Then, we consider 1000 system snapshots uniformly distributed in time over an additional top-wall shear displacement of $250H$. Anticipating that the velocity and stress fields are homogeneous along the x-direction, we average along the x-direction at discrete z-positions for each snapshot. We utilize the spatial averaging technique described by Koval and coworkers,[11,25] which is briefly summarized in Appendix A. The instantaneous velocity and stress fields are then arithmetically averaged over all snapshots to obtain steady fields that depend only upon the z-coordinate. In all cases of planar shear flow, the steady velocity field $v_x(z)$ is linear with very little wall slip, allowing us to define a corresponding, spatially-constant shear strain-rate $\dot{\gamma} = |\mathrm{d}v_x/\mathrm{d}z|$. All stress components are spatially constant as well. Moreover, the normal stresses σ_{xx} and σ_{zz} are approximately equal. Therefore, the shear stress and pressure may be denoted as $\tau = |\sigma_{xz}| = |\sigma_{zx}|$ and $P = -\sigma_{zz} \approx -\sigma_{xx}$, respectively, and we may calculate the inertial number $I = \dot{\gamma}\sqrt{m/P}$ and stress ratio $\mu = \tau/P$ corresponding to each prescribed wall velocity. The relationship between μ and I extracted from our DEM simulations is plotted in Fig. 1(b) as gray symbols, along with the DEM data of da Cruz *et al.*[2] and Kamrin and Koval[25] for stiff, frictional disks with $\mu_{\text{surf}} = 0.4$ as black symbols. The DEM results are consistent, verifying our methodology. The DEM data for two-dimensional granular systems consisting of disks may be fit by a simple Bingham-like functional form of the inertial rheology:[2]

$$\mu_{\text{loc}}(I) = \mu_s + bI, \tag{1}$$

where μ_s and b are dimensionless material parameters. The relation (1) – using fitted parameter values of $\mu_s = 0.272$ and $b = 1.168$ – is plotted in Fig. 1(b), demonstrating that the linear form (1) captures DEM data for homogeneous planar shear.

3 Granular rheology and the flow threshold

In this section, we discuss the nonlocal granular fluidity model for steady, dense granular flow and its attendant description of the flow threshold. Motivated by experimental observations of cooperative effects, a number of nonlocal continuum approaches have been pursued. For example, Ginzberg–Landau theories based on a partial-fluidization order parameter[17] or the inertial number[20] and extensions of kinetic theory[23] have been used to make predictions of the flow threshold for inclined plane flow. Recently, an alternative nonlocal continuum model for dense granular flow, based on the concept of "granular fluidity" – a concept inspired by nonlocal fluidity models for emulsions[27,28] – has shown promise in capturing cooperative effects observed in experiments, including flow fields in a variety of boundary-driven and gravity-driven flows,[18,29,30] the secondary rheology of intruders,[31] as well as the thickness-dependence of the flow threshold in inclined plane flow.[24]

§ Experience tells us that flow typically reaches steady state within a top-wall shear displacement of $100H$ after a short transient.

In the NGF model, a positive, scalar field quantity – the granular fluidity – is introduced and denoted as g. The works of Zhang and Kamrin[32] and Bhateja and Khakhar[33] have established that the granular fluidity has an unambiguous kinematic definition that holds across a wide variety of inhomogeneous flow configurations and is given through the relation $g = (\delta v/d)F(\phi)$, where δv is the velocity fluctuation, ϕ is the solid fraction, d is the grain size, and $F(\phi)$ is a function of only ϕ. Then, instead of relating the stress state to the strain-rate through a single constitutive equation as in the inertial rheology (1), the NGF model relates the stress state, the strain-rate, and the granular fluidity through two constitutive equations as follows:

$$\dot{\gamma} = g\mu, \tag{2}$$

$$t_0\dot{g} = A^2 d^2 \nabla^2 g - (\mu_s - \mu)g - b\sqrt{\frac{m}{P}}\mu g^2, \tag{3}$$

where $t_0 > 0$ is a constant timescale associated with the dynamics of g, $A > 0$ is a constant dimensionless material parameter characterizing nonlocal effects, called the nonlocal amplitude, and the dimensionless constants μ_s and b are the same as those appearing in the local inertial rheology (1). The duel constitutive roles of the granular fluidity become clear in (2) and (3). First, in (2), g operates as a fluidity-like quantity, relating the stress ratio μ to the consequent shear strain-rate $\dot{\gamma}$, and second, in (3), g operates as a nonlocal order parameter governed by a dynamical system – in a manner that bears a mathematical similarity to other Ginzberg–Landau-based approaches.[17,20] When the flow field is homogeneous ($\nabla^2 g = 0$), the granular fluidity evolves to the stable, steady, stress-dependent solution of the dynamical system (3), which is given by

$$g_{\mathrm{loc}}(\mu, P) = \begin{cases} \sqrt{\dfrac{P}{m}}\dfrac{(\mu - \mu_s)}{b\mu} & \text{if } \mu > \mu_s, \\ 0 & \text{if } \mu \leq \mu_s, \end{cases} \tag{4}$$

and referred to as the local fluidity. When the granular fluidity is given through (4) and combined with (2), the local inertial rheology (1) is recovered, and hence, the NGF model reduces to the inertial rheology for steady, homogeneous flow. However, when flow gradients are present, the Laplacian term in (3) introduces an intrinsic length-scale given through the grain size d, and the NGF model produces nonlocal predictions.

Several comments on the dynamical relation (3) are in order:

1. As discussed in Henann and Kamrin,[34] the last two terms in (3) arise through the derivative of a coarse-grain Ginzburg–Landau-type free energy. Since these terms then determine the stable, steady solution for g in the absence of flow gradients – *i.e.*, the local fluidity (4) – the choices of the Ginzburg–Landau-type free energy and the fitting function for the local inertial rheology are one and the same. Hence, if one were to utilize a different functional form for the inertial rheology than the Bingham-like form (1), it would be necessary to modify these terms in (3). Indeed, as I increases, deviation from the linear form (1) is often observed, leading to the use of nonlinear fitting functions.[3,35] In our previous work applying the NGF model to dense flows of spheres down inclines,[24] we chose to work with the commonly-utilized, nonlinear fitting function of Jop *et al.*,[35] which involves an upper-limiting value of μ, and hence, the dynamical relation (3) took on a slightly different form. In the present work, focusing on two-dimensional granular systems of disks, the Bingham-like form of the inertial rheology works well up to a stress ratio of 0.5 (see Fig. 1(b)), so we utilize the corresponding dynamical form (3), while limiting attention to situations in which the stress ratio remains less than 0.5.

2. The dynamics embodied by (3) does not involve bistability, in which two stable, steady-state values of g exist for some range of μ. This feature would lead to a non-monotonic local rheology and hysteresis of the predicted flow threshold. There is some experimental evidence for a non-monotonic local rheology in dense flows of spheres;[36] however, non-monotonicity is not observed in our DEM simulations of disks, so we neglect the possibility of this effect in the present work.

3. The time-dependent term appearing in (3) is not intended to quantitatively describe the approach to steady state, such as the transient variations in flow resistance that accompany Reynolds dilatancy or the transient effects reported by Ries *et al.*[37] However, the model does provide an accurate description of the long-term dynamical behavior – *i.e.*, steady flow – as well as the flow threshold. In these cases, the numerical value of the positive parameter t_0 appearing in (3) is irrelevant.

4. The differential relation (3) may be reduced to a steady-state-only form under the approximation that deviations of the granular fluidity g from the local fluidity g_{loc} are small. The result of such an approximation – the details of which are discussed in Henann and Kamrin[34] – is

$$g = g_{\mathrm{loc}} + \xi^2 \nabla^2 g \quad \text{with} \quad \xi(\mu) = \frac{Ad}{\sqrt{|\mu - \mu_s|}}, \tag{5}$$

where $g_{\mathrm{loc}}(\mu,P)$ is the local fluidity function (4) and $\xi(\mu)$ is a stress-dependent length-scale called the cooperativity length. The steady-state form of the NGF model (5) may be straightforwardly applied to obtain accurate predictions of non-uniform steady flow fields in a variety of geometric configurations, such as split-bottom flow[29] and chute flow.[30] However, (5) cannot capture the size-dependence of the flow threshold. To see this, note that the local fluidity function (4) mathematically acts as a source term in (5) and is non-zero whenever $\mu > \mu_s$. Then, when μ exceeds μ_s at any point in a dense granular medium, (5) will predict flowing solutions, regardless of the size of the granular medium. This deficiency arises because the approximation that g is close to g_{loc} breaks down as the size of a granular medium decreases. For example, in dense granular flows down an incline, flow arrests in thin layers when μ is significantly greater than μ_s and hence g_{loc} is significantly greater than zero. Therefore, to obtain predictions of the size-dependence of the flow threshold, we utilize the primitive, dynamical form of the NGF model (3) exclusively throughout the remainder of this paper.

Next, we discuss how predictions of the flow threshold may be obtained from the NGF model. For the local inertial rheology, the flow threshold is determined by simply comparing

the maximum value of the stress ratio μ occurring in a flow configuration to the critical value μ_s. However, for the nonlocal model (3), this method of assessing the flow threshold is no longer sufficient. Instead, we reframe the question of whether or not steady flow is possible as whether or not the $g = 0$ solution is linearly stable under perturbation. Starting from (3) and linearizing about the $g = 0$ solution renders the g^2 term negligible, and we assume a perturbed solution $\hat{g}$ of the form $\hat{g}(\mathbf{x},t) = C\exp(\lambda t/t_0)\breve{g}(\mathbf{x})$, where λ is the dimensionless growth rate of the perturbation, $\breve{g}(\mathbf{x})$ is a time-independent function, $\mathbf{x}$ is the spatial coordinate, and C is an arbitrary constant. Substituting the perturbed solution $\hat{g}$ into the linearized form of (3) and simplifying, we obtain the following linear differential relation for $\breve{g}$:

$$A^2d^2\nabla^2\breve{g} - (\lambda + \mu_s - \mu)\breve{g} = 0. \tag{6}$$

Then, for a given flow configuration, the field $\mu(\mathbf{x})$ is specified along with appropriate homogeneous boundary conditions for $\breve{g}$, and the growth rate λ may be calculated. If $\lambda < 0$, the perturbation decays, and steady flow is not possible. If $\lambda > 0$, the perturbation grows, and steady flow may occur. The flow threshold may be identified as the case in which $\lambda = 0$. In subsequent discussions of the theoretically predicted flow threshold, we denote $\breve{g}$ as g for notational simplicity.

The NGF-model-predicted flow threshold for inclined plane flow has been derived in our previous work.[24] Here, we briefly recap the linear perturbation process that will subsequently be applied to the more complex flow configurations in Section 4. The μ-field in inclined plane flow is spatially constant and given through the angle of inclination by $\tan\theta$, *i.e.*, $\mu = \tan\theta$. Therefore, (6) takes the form of an ordinary differential equation (ODE) with constant coefficients:

$$\frac{\mathrm{d}^2g}{\mathrm{d}z^2} + \left(\frac{\tan\theta - \lambda - \mu_s}{A^2d^2}\right)g = 0, \tag{7}$$

where z is the distance from the free surface. Anticipating that the quantity $(\tan\theta - \lambda - \mu_s)$ is positive, the solution to (7) is $g = C_1\sin[(\sqrt{\tan\theta - \lambda - \mu_s}/Ad)z] + C_2\cos[(\sqrt{\tan\theta - \lambda - \mu_s}/Ad)z]$, where C_1 and C_2 are arbitrary constants. As discussed in our previous work,[24] the choice of homogeneous boundary conditions is important. For inclined plane flow, we based this choice on observations of existing DEM flow data of spheres.[7] In particular, in the region near the free surface ($z = 0$), the DEM data of Silbert *et al.*[7] shows that the strain-rate approximately levels off, implying a zero strain-rate gradient. Accordingly, we enforce that $\mathrm{d}g/\mathrm{d}z = 0$ at $z = 0$, which requires that $C_1 = 0$. Second, Silbert *et al.*[7] observed that adjacent to a fully rough boundary, the strain-rate approaches an approximately vanishing state, and hence, we take $g = 0$ at $z = H$. The lowest value of $\tan\theta$ that satisfies this boundary condition corresponds to

$$\frac{H}{d} = \frac{\pi}{2}\frac{A}{\sqrt{\tan\theta - \mu_s}}. \tag{8}$$

In (8), λ has been set to zero, so that (8) represents the size-dependent flow threshold for inclined plane flow. For thick layers, the flow threshold approaches the size-independent value $\tan\theta = \mu_s$; however, for thinner layers, flow ceases at higher inclination angles. To obtain the flow thresholds corresponding to the more complex flow configurations considered in Section 4, we apply the same linear perturbation process – albeit involving more complex stress ratio fields. The details of these calculations and the resulting theoretical flow thresholds are given in Section 4.

A deeper discussion of the role of fluidity boundary conditions in NGF model predictions of the flow threshold is warranted. In the case of inclined plane flow, it is the choice of a homogeneous Dirichlet fluidity boundary condition at the rough base that leads to predictions of size-dependent strengthening. Indeed, if a homogeneous Neumann condition were employed, a size-independent angle of repose would be predicted. However, as will be shown in Section 4, NGF model predictions of size-dependent strengthening do not arise solely due to wall conditions. In a flow configuration with a spatially varying μ-field, in which some spatial regions experience $\mu > \mu_s$ while others experience $\mu < \mu_s$, the NGF model also predicts size-dependent strengthening, regardless of the choice of wall boundary condition. In such a case, the region experiencing $\mu < \mu_s$ serves to stabilize the region experiencing $\mu > \mu_s$ through nonlocal effects, while a local model would simply predict the region experiencing $\mu > \mu_s$ to flow. The flow configurations considered in Section 4 involve both spatially varying μ-fields and rough walls. In the DEM simulations reported in Section 4, we are unable to extract clear evidence justifying a homogeneous Dirichlet boundary condition for the fluidity at walls. Therefore, for the sake of simplicity, following our previous work,[29–31] we employ homogeneous Neumann fluidity boundary conditions at walls throughout – both in calculating theoretical flow thresholds and steady flow fields. We note that a similar choice of wall fluidity boundary condition was employed by Chaudhuri *et al.*[38] in their investigation of vertical chute flow of soft, frictionless disks. In spite of this rather naive choice of fluidity boundary condition, the results of Section 4 demonstrate that good agreement between DEM data and NGF model predictions may be obtained, indicating that the specifics of the stress field may play a larger role than wall conditions.

4 Flow threshold in other configurations

In this section, we present DEM simulation results in three flow configurations – planar shear flow with gravity, annular shear flow, and vertical chute flow – characterizing the size-dependence of the flow threshold in each case. To be clear, in the context of our DEM simulations, the flow threshold refers to the condition for flow cessation and not the condition for flow start-up, which is typically greater than the flow cessation condition and is dependent on the preparation history. In this section, we also compare DEM results with corresponding predictions of the NGF model. Throughout, we use a single set of material parameters $\{\mu_s, b, A\}$ in obtaining NGF model predictions. Based on the fit of the Bingham-like functional form of the inertial rheology (1) to

DEM data of homogeneous planar shearing (Fig. 1(b)), we utilize local parameter values of $\mu_s = 0.272$ and $b = 1.168$. In contrast, the nonlocal amplitude is not obtained by fitting to a single data set – rather, we choose a value of $A = 0.90$ in order to provide the best collective description of all subsequently reported data. We note that this numerical value is similar to the value $A = 0.80$, which was reported by Kamrin and Koval[25] for disks with an inter-particle sliding friction coefficient $\mu_{surf} = 0.4$.

4.1 Planar shear flow with gravity

First, we consider planar shear flow with gravity acting orthogonal to the shearing direction. We note that size-dependent strengthening in this configuration was first suggested by Pouliquen and Forterre[16] in the context of their modeling work, but to our knowledge, this effect has not been reported in experiments or DEM simulations. The DEM set-up for this case is shown in Fig. 2(a) and is achieved by introducing a gravitational body force along the z-direction to the configuration used in planar shear flow, described in Section 2.2. The parallel, rough walls are separated by a distance $H = 60d$, and the top wall moves in the x-direction with a velocity v_{wall}, while the bottom wall remains fixed. The top wall imposes a compressive normal stress P_{wall} on the granular material, using the control procedure described in Section 2.2, and the gravitational body force is $\phi\rho_s G$, where ϕ is the mean solid area fraction and G is the acceleration of gravity. Periodic boundary conditions are employed along the x-direction, and the length of the region in the x-direction is $L = 60d$.

The expected stress field in this flow configuration may be deduced from a quasi-static force balance. As in planar shear flow without gravity, the shear stress is spatially constant and given by the shear stress imparted by the moving wall – *i.e.*, $\tau(z) = |\sigma_{xz}(z)| = |\sigma_{zx}(z)| = \tau_{wall}$. The pressure field is a combination of the prescribed wall pressure P_{wall} and the gravitational pressure gradient, so that $P(z) = -\sigma_{zz}(z) = P_{wall} + \phi\rho_s G z$. As in planar shear flow, we assume that $\sigma_{xx}(z) \approx \sigma_{zz}(z)$, which is consistent with the results of our DEM simulations. Therefore, the stress ratio field in planar shear flow with gravity varies as

$$\mu(z) = \frac{\tau(z)}{P(z)} = \frac{\mu_{wall}}{1 + z/\ell}, \tag{9}$$

where $\mu_{wall} = \tau_{wall}/P_{wall}$ is the maximum value of μ, occurring at the wall ($z = 0$), and $\ell = P_{wall}/\phi\rho_s G$ is the loading length-scale, which is defined as the ratio of the wall pressure to the gravitational body force and is distinct from the dimensions H and L. Importantly, since the loading length-scale ℓ is the only length-scale appearing in the stress ratio field (9), ℓ – rather than the dimensions H or L – is the relevant length-scale that characterizes the system size in this problem. The loading length-scale ℓ may be interpreted as the distance beneath the

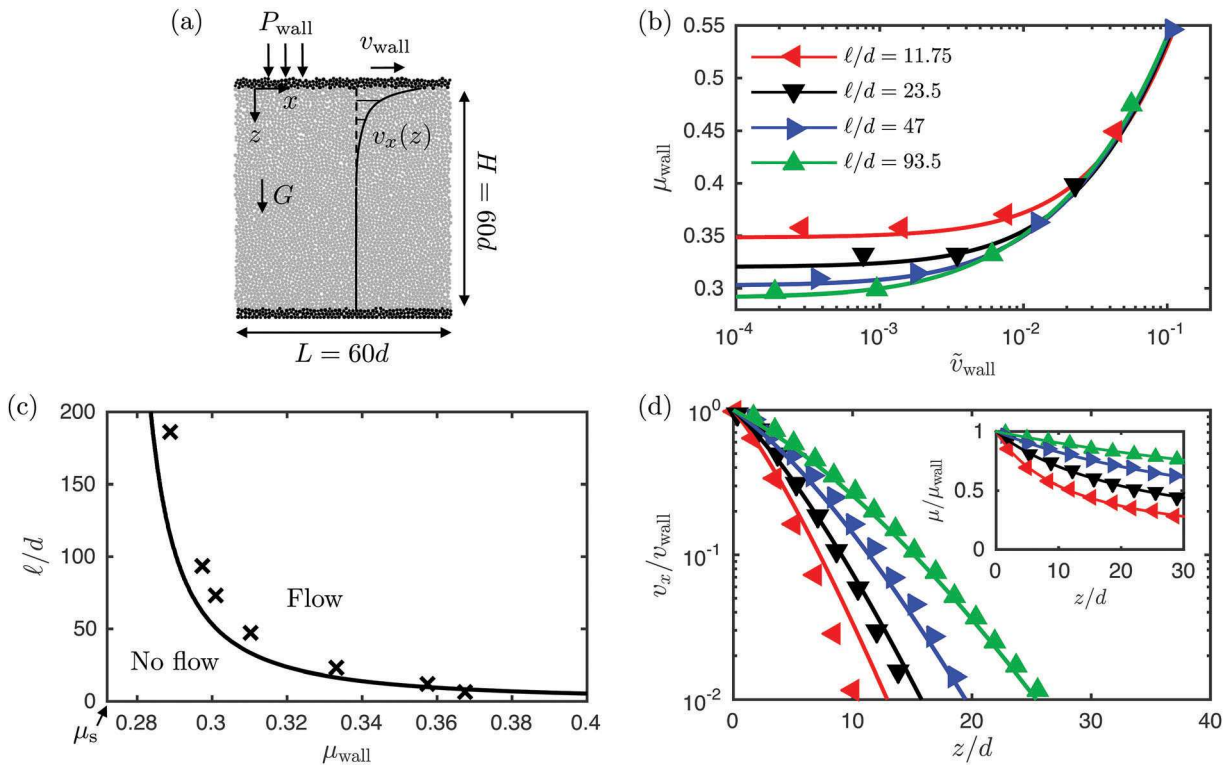

Fig. 2 (a) Configuration for two-dimensional DEM simulations of planar shear flow with gravity. (b) The dependence of the stress ratio at the wall μ_{wall} on $\tilde{v}_{wall}$ for loading length-scales $\ell/d = P_{wall}/\phi\rho_s G d = 11.75$, 23.5, 47, and 93.5. (c) Flow threshold locus. (d) Normalized steady velocity fields in the plateau regime ($\tilde{v}_{wall} \approx 10^{-3}$) for the four loading length-scales in (b). Inset: Steady stress ratio fields corresponding to each case. Throughout, symbols represent the steady-state results of DEM simulations. In (b and d), solid lines are the calculated steady results of the NGF model, (2) and (3). In (c), the solid line is the analytical flow threshold predicted by the NGF model (12). In the inset of (d), the solid lines are the anticipated μ-fields (9) used as input in calculations involving the NGF model.

top wall at which the pressure due to gravity $\phi\rho_s G\ell$ is equal to the pressure applied by the top wall P_{wall} – *i.e.*, $P(z = \ell) = 2P_{wall}$. We have verified that the dimensions $H = 60d$ and $L = 60d$ are sufficiently large so that they do not affect the subsequently reported DEM results.

We run DEM simulations of planar shear flow with gravity for different values of the top-wall speed v_{wall} and loading length-scale ℓ. Each DEM simulation is run to steady state through a top-wall shear displacement of at least $5500d$, and the steady fields $v_x(z)$, $\tau(z)$, and $P(z)$ are calculated using 2000 system snapshots – evenly spaced over an additional top-wall shear displacement of at least $5500d$ – as described in Appendix A. In each case, we verify that the resulting shear stress field is indeed constant – thereby extracting the corresponding value of τ_{wall} – and that the pressure field matches the intended dependence $P(z) = P_{wall} + \phi\rho_s Gz$. In presenting results, we utilize a dimensionless wall velocity $\tilde{v}_{wall} = (v_{wall}/\ell)\sqrt{m/P_{wall}}$, in which v_{wall} is non-dimensionalized through the loading length-scale and the microscopic time-scale associated with particle motion. First, we probe the dependence of the stress ratio at the wall $\mu_{wall} = \tau_{wall}/P_{wall}$ on $\tilde{v}_{wall}$ for loading length-scales $\ell/d = 11.75$, 23.5, 47, and 93.5, which is plotted as symbols in Fig. 2(b). For sufficiently high wall speed – *i.e.*, $\tilde{v}_{wall} \gtrsim 3 \times 10^{-2}$ – the relationship between μ_{wall} and $\tilde{v}_{wall}$ is size-independent, indicating that the response is dominated by local, inertial effects. However, as the wall speed is decreased, a rate-independent plateau emerges, which is dependent on the system-size ℓ/d. Therefore, for a given ℓ/d, steady flow is not possible for μ_{wall} less than the plateau value, enabling the construction of a phase diagram of flowing and non-flowing states. As shown in Fig. 2(c), we create a phase diagram with ℓ/d on the vertical axis and μ_{wall} on the horizontal axis. Then, the DEM-calculated flow threshold locus is plotted as symbols on the phase diagram – in which each point consists of a given ℓ/d and the corresponding plateau value of μ_{wall}. Steady flow is possible for combinations of ℓ/d and μ_{wall} to the right of the flow threshold locus, while steady flow cannot occur for combinations to the left of the locus. For a large system-size, the flow threshold approaches the size-independent value μ_s; however, as ℓ/d decreases the flow threshold increases.

We have also numerically computed corresponding steady solutions of the NGF model, (2) and (3). Model predictions of steady velocity fields are calculated for a given combination of ℓ/d and μ_{wall}, by evolving (3) to steady state, using finite differences in MATLAB with μ-field given through (9), a very fine spatial resolution $\Delta z \ll d$, and the solution of (5) as the initial guess. The calculated relationships between the wall stress ratio μ_{wall} and the dimensionless wall speed $\tilde{v}_{wall}$ are plotted as solid lines in Fig. 2(b) for $\ell/d = 11.75$, 23.5, 47, and 93.5. The NGF model quantitatively captures both the size-independent but rate-dependent regime observed in DEM simulations at sufficiently high wall speed and the size-dependent but rate-independent plateau regime – an observation that may be understood in terms of the dynamical relation (3) as follows. At sufficiently high wall speed, the Laplacian term in (3) contributes negligibly, yielding size-independent model predictions. Consequently, the parameters μ_s and b – but not A – set the model predictions in the rate-dependent regime. In contrast, for sufficiently slow flows, the g^2 term plays a negligible role, rendering the dynamical relation (3) linear in g which leads to rate-independent model predictions. The parameters μ_s and A – but not b – determine NGF model predictions in the rate-independent regime.

The plateau value of μ_{wall} calculated using the NGF model for a given value of ℓ/d then represents a point on the predicted flow threshold locus. Instead of constructing the locus using discrete points determined in this way, we have calculated the analytical flow threshold predicted by the NGF model for planar shear flow with gravity using the linear perturbation procedure described in Section 3. We define a dimensionless transformed coordinate $\tilde{z}$ and a positive, dimensionless constant α as

$$\tilde{z} = 2\sqrt{\lambda + \mu_s}\frac{(z+\ell)}{Ad} \quad \text{and} \quad \alpha = \frac{\mu_{wall}}{2\sqrt{\lambda+\mu_s}}\frac{\ell}{Ad}. \tag{10}$$

Then, upon substituting the μ-field for planar shear flow with gravity (9) into (6), the resulting linear ODE for $g(\tilde{z})$ is

$$\frac{d^2 g}{d\tilde{z}^2} + \left(-\frac{1}{4} + \frac{\alpha}{\tilde{z}}\right)g = 0. \tag{11}$$

The solution of (11) is $g = C_1 M_{\alpha,1/2}(\tilde{z}) + C_2 W_{\alpha,1/2}(\tilde{z})$, where $M_{\alpha,1/2}(\tilde{z})$ and $W_{\alpha,1/2}(\tilde{z})$ are Whittaker functions, and C_1 and C_2 are constants. The homogeneous boundary conditions consist of a Neumann condition at the moving wall, $dg/dz|_{z=0} = 0$, and the far-field boundary condition, $\lim_{z\to\infty} g = 0$. Since the function $M_{\alpha,1/2}(\tilde{z})$ diverges as $\tilde{z} \to \infty$, while $W_{\alpha,1/2}(\tilde{z}) \to 0$, the far-field boundary condition requires that $C_1 = 0$. Then, applying the wall boundary condition, making use of the identity $W_{\alpha,1/2}'(\tilde{z}) = ((\tilde{z} - 2\alpha)W_{\alpha,1/2}(\tilde{z}) - 2W_{\alpha+1,1/2}(\tilde{z}))/2\tilde{z}$, and simplifying, we obtain

$$\left(\sqrt{\mu_s}\frac{\ell}{Ad} - \alpha\right)W_{\alpha,1/2}\left(2\sqrt{\mu_s}\frac{\ell}{Ad}\right) - W_{\alpha+1,1/2}\left(2\sqrt{\mu_s}\frac{\ell}{Ad}\right) = 0 \quad \text{with} \quad \alpha = \frac{\mu_{wall}}{2\sqrt{\mu_s}}\frac{\ell}{Ad}. \tag{12}$$

In the above expression, we have set λ to the threshold value of $\lambda = 0$, so that (12) represents the size-dependent flow threshold for planar shear with gravity. For a given value of the dimensionless system size ℓ/d and the material parameters μ_s and A, the smallest, positive value of μ_{wall} that satisfies the transcendental eqn (12) gives the flow threshold. The analytical flow threshold (12) is plotted as a solid line in Fig. 2(c) – displaying a favorable quantitative comparison with the DEM data.

Finally, we compare steady velocity fields extracted from DEM simulations to corresponding NGF model predictions. Steady normalized velocity fields $v_x(z)/v_{wall}$ in the plateau regime ($\tilde{v}_{wall} \approx 10^{-3}$) for loading length-scales $\ell/d = 11.75$, 23.5, 47, and 93.5 are shown in Fig. 2(d) with symbols denoting DEM data and solid lines representing NGF model predictions. In the inset of Fig. 2(d), symbols denote the corresponding normalized stress ratio fields $\mu(z)/\mu_{wall}$ measured in the DEM simulations, and solid lines represent the anticipated stress ratio fields (9) used as input in calculations involving the NGF

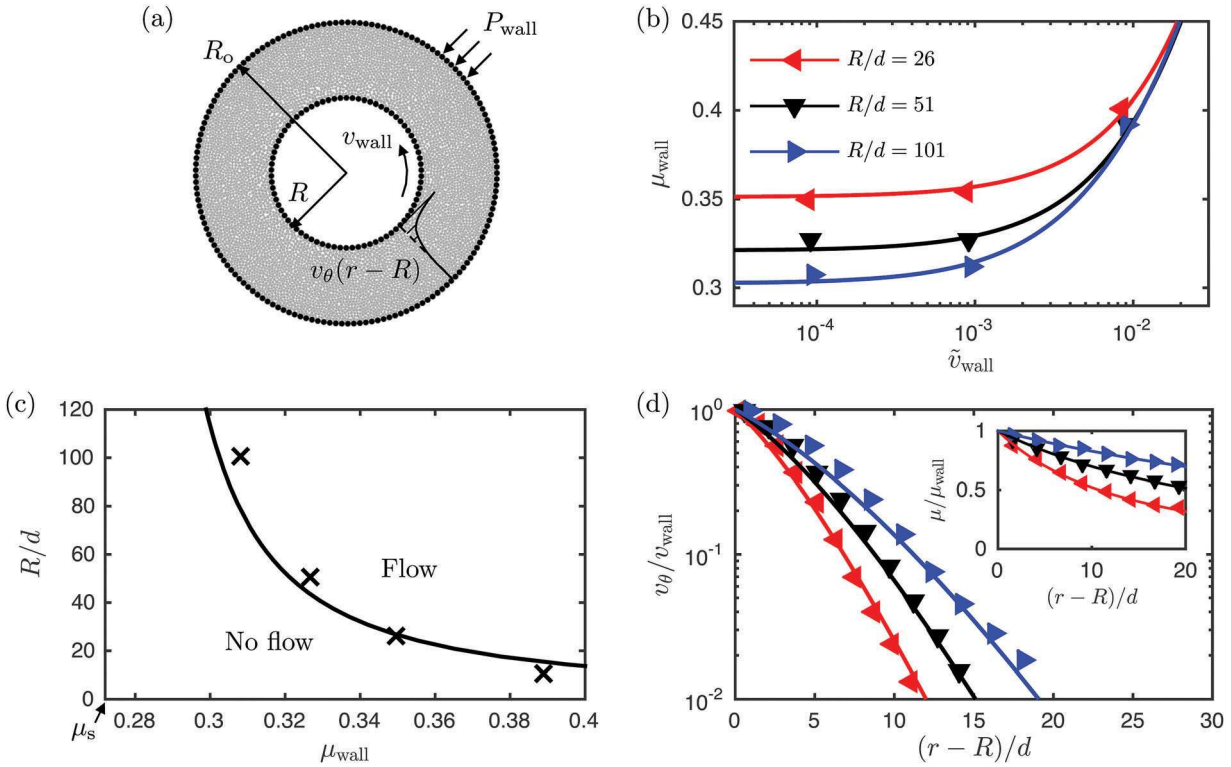

Fig. 3 (a) Configuration for two-dimensional DEM simulations of annular shear flow for the case of $R/d = 26$. (b) The dependence of the stress ratio at the wall μ_{wall} on $\tilde{v}_{\text{wall}}$ for inner wall radii $R/d = 26$, 51, and 101. (c) Flow threshold locus. (d) Normalized steady velocity fields in the quasi-static regime ($\tilde{v}_{\text{wall}} \approx 10^{-4}$) for the three loading length-scales in (b). Inset: Steady stress ratio fields corresponding to each case. Throughout, symbols represent the steady-state results of DEM simulations. In (b and d), solid lines are the calculated steady results of the NGF model, (2) and (3). In (c), the solid line is the analytical flow threshold predicted by the NGF model (16). In the inset of (d), the solid lines are the anticipated μ-fields (13) used as input in calculations involving the NGF model.

model, confirming that the intended stress fields are achieved in the DEM simulations. Overall, the NGF model is able to quantitatively capture the salient aspects of the flow fields in planar shear flow with gravity over a range of loading length-scales. Importantly, the nonlocal amplitude A is the operative material parameter that determines NGF model predictions of steady flow fields in the plateau regime, and using a single numerical value of A, the NGF model simultaneously captures DEM data of both the size-dependence of the flow threshold and steady flow fields.

4.2 Annular shear flow

Next, we consider annular shear flow – the DEM set-up for which is shown in Fig. 3(a) with inner radius R and outer radius R_0. For the most part, the details of our DEM simulations of annular shear flow follow the procedures of Koval and coworkers.[11,25] The walls in our DEM simulations of annular shear flow consist of rings of glued grains of diameter $2d$,¶ and the inner radius R corresponds to the radial position of the outermost points of the inner wall grains. At the inner wall, we prescribe the circumferential wall velocity v_{wall}, and the radial position of the inner wall grains is fixed. While the outer wall does not rotate, the value of R_0 fluctuates slightly so as to impose a prescribed radial compressive normal stress P_{wall} on the granular material, using a control procedure analogous to that used in Section 2.2 and described by Koval *et al.*[11] We do not utilize periodic boundary conditions, instead modeling the full annular shear cell, as shown in Fig. 3(a) for the case of $R/d = 26$. In total, we consider inner wall radii of $R/d = 11$, 26, 51, and 101. Throughout, we take the outer radius to be sufficiently large so that the value of R_0 does not affect the subsequently reported results – $R_0 = 2R$ for $R/d = 26$, 51, and 101 and $R_0 = 4R$ for $R/d = 11$. The DEM configurations for $R/d = 11$, 26, 51, and 101 contain 4640, 5715, 23 900, and 97 696 flowing grains, respectively.

Analogous to planar shear with gravity, we may deduce the steady stress field from quasi-static force and moment balances. The moment balance gives the shear stress field to be $\tau(r) = |\sigma_{r\theta}(r)| = |\sigma_{\theta r}(r)| = \tau_{\text{wall}}(R/r)^2$, where r is the radial coordinate and τ_{wall} is the inner wall shear stress, and the radial force balance gives that $P(r) = -\sigma_{rr}(r) = P_{\text{wall}}$ is spatially constant. Again, we assume that the normal stresses are equal – *i.e.*, $\sigma_{\theta\theta} \approx \sigma_{rr}$ – which is consistent with DEM simulation results. Therefore, for annular shear flow, the stress ratio field varies as

$$\mu(r) = \frac{\tau(r)}{P(r)} = \mu_{\text{wall}}\left(\frac{R}{r}\right)^2, \qquad (13)$$

¶ Rough walls consisting of glued grains of diameter $2d$ were also used in the annular shear flow simulations of Kamrin and Koval.[25] We utilize this type of rough wall for our annular shear flow simulations rather than the rough walls described in Section 2.2 in order to more easily construct the annular DEM configuration.

where $\mu_{wall} = \tau_{wall}/P_{wall}$ is the maximum value of μ, occurring at the inner wall ($r = R$).

Our discussion of simulation results for annular shear flow mirrors that of Section 4.1 for planar shear flow with gravity. We run DEM simulations for different values of the inner wall speed v_{wall} and radius R. Each simulation is first run to steady state through an inner-wall tangential displacement of at least $48d$,‖ and the steady fields $v_\theta(r)$, $\tau(r)$, and $P(r)$ are then extracted using 1000 system snapshots, which are evenly spaced over an additional inner-wall tangential displacement of an equal amount as in the preceding step. Further, τ_{wall} is measured by way of the average torque applied to the inner wall at steady state. First, we explore the dependence of the inner wall stress ratio μ_{wall} on $\tilde{v}_{wall} = (v_{wall}/R)\sqrt{m/P_{wall}}$ in DEM simulations for R/d = 26, 51, and 101, which is plotted as symbols in Fig. 3(b). Again, a transition is observed from a rate-dependent but size-independent regime at sufficiently high wall speed ($\tilde{v}_{wall} \gtrsim 10^{-2}$) to a size-dependent plateau regime as $\tilde{v}_{wall}$ is decreased. Here, we have restricted attention to a slightly lower range of $\tilde{v}_{wall}$ than considered in Section 4.1 to ensure that centripetal acceleration plays no role in our DEM simulations – a point which is verified by checking that the normal stress σ_{rr} is spatially constant. A phase diagram of flowing and non-flowing states for annular shear flow is shown in Fig. 3(c), in which pairs of R/d and the corresponding plateau value of μ_{wall} are plotted as symbols and denote the DEM-calculated flow threshold locus. Again, we observe strengthening as the system-size R/d is reduced.

Steady-state predictions of the NGF model are numerically calculated for given combinations of R/d and μ_{wall} as described in Section 4.1 except with μ-field given through (13). The calculated relationships between μ_{wall} and $\tilde{v}_{wall}$ are plotted as solid lines in Fig. 3(b) for R/d = 26, 51, and 101, demonstrating good quantitative agreement with DEM data and – most importantly – displaying a size-dependent plateau value of μ_{wall}. As in Section 4.1, we calculate the theoretical flow threshold locus for annular shear flow *via* the linear perturbation procedure described in Section 3. Substituting the μ-field (13) into (6), defining a dimensionless transformed coordinate $\tilde{r}$ and a positive, dimensionless constant α as

$$\tilde{r} = \sqrt{\lambda + \mu_s}\frac{r}{Ad} \quad \text{and} \quad \alpha = \sqrt{\mu_{wall}}\frac{R}{Ad}, \tag{14}$$

and simplifying, we obtain the following linear ODE for $g(\tilde{r})$:

$$\tilde{r}^2\frac{d^2g}{d\tilde{r}^2} + \tilde{r}\frac{dg}{d\tilde{r}} - (\tilde{r}^2 - \alpha^2)g = 0. \tag{15}$$

The solution of (15) is $g = C_1 I_{i\alpha}(\tilde{r}) + C_2 K_{i\alpha}(\tilde{r})$, where $I_{i\alpha}(\tilde{r})$ and $K_{i\alpha}(\tilde{r})$ are the modified Bessel functions of the first and second kind of purely imaginary order, and C_1 and C_2 are constants. We consider the following homogeneous boundary conditions: a Neumann condition at the inner wall, $dg/dr|_{r=R} = 0$, and the far-field condition, $\lim_{r\to\infty} g = 0$. For $\tilde{r}$ and α positive, the function $I_{i\alpha}(\tilde{r})$ is complex-valued, and its real part diverges as $\tilde{r} \to \infty$. In contrast, $K_{i\alpha}(\tilde{r})$ is real-valued for $\tilde{r}$ and α positive, and $K_{i\alpha}(\tilde{r}) \to 0$ as $\tilde{r} \to \infty$. Therefore, the far-field boundary condition requires that $C_1 = 0$. Then, applying the wall boundary condition, setting $\lambda = 0$, and simplifying leads to the size-dependent flow threshold for annular shear flow:

$$K_{i\alpha}{}'\left(\sqrt{\mu_s}\frac{R}{Ad}\right) = 0 \quad \text{with} \quad \alpha = \sqrt{\mu_{wall}}\frac{R}{Ad}. \tag{16}$$

For a given value of the dimensionless inner wall radius R/d and the material parameters μ_s and A, the smallest, positive value of μ_{wall} that satisfies (16) gives the flow threshold. The theoretical flow threshold locus (16) is plotted as a solid line in Fig. 3(c), showing that the NGF model captures the size-dependent flow threshold in this flow configuration.

Lastly, we compare DEM data and NGF model predictions of steady velocity fields. Steady normalized velocity fields $v_\theta(r)/v_{wall}$ in the plateau regime ($\tilde{v}_{wall} \approx 10^{-4}$) for inner wall radii R/d = 26, 51, and 101 are shown in Fig. 3(d) with symbols denoting DEM data and solid lines representing NGF model predictions. Corresponding steady normalized stress ratio fields $\mu(r)/\mu_{wall}$ are shown in the inset of Fig. 3(d), confirming that the μ-fields measured from DEM data are consistent with the anticipated stress ratio fields (13). The NGF model quantitatively captures both steady flow fields and the size-dependence of the flow threshold in annular shear flow – while using the same set of material parameters as in planar shear flow with gravity.

4.3 Vertical chute flow

Finally, we consider vertical chute flow. The size-dependence of the flow threshold in this configuration was first explored by Chaudhuri *et al.*[38] for a simulated, two-dimensional system of soft, frictionless particles. Here, we perform an analogous analysis for our system of stiff, frictional disks. Our DEM set-up is shown in Fig. 4(a), which is generated by first creating a dense granular system between two parallel, rough walls as described for planar shear in Section 2.2 and then rotating the system clockwise by 90° and applying a gravitational body force along the z-direction. The rough walls – consisting of layers of glued grains as in the planar shear flow simulations of Section 2.2 – are separated by a distance denoted by W, which is varied in our simulations. The left vertical wall is fixed, and the right vertical wall is fixed in the z-direction but can move slightly in the x-direction so as to impose a compressive normal stress P_{wall} on the granular material, using the control procedure described in Section 2.2. Periodic boundary conditions are prescribed along the z-direction. In all cases, the length of the vertical chute L is taken to be $60d$, which is in a range that does not affect DEM results.** We consider nominal chute widths of

‖ Koval and coworkers[11,25] report that transients fully subside after an inner-wall tangential displacement of approximately $50d$ in their simulations of annular shear flow and conservatively adopt an inner-wall displacement of $100d$ as their steady-state condition. Our observation of transients is similar, and for efficiency – since we simulate the full annular shear cell rather than an angular section – we adopt a steady-state condition of $48d$ for the inner-wall displacement.

** If the vertical chute is taken to be too long, alternating dense and sparse regions will develop along the chute. This is because the procedure employed to control the pressure cannot account for variations along the length of the vertical chute due to the rigid nature of the walls. We have verified that our chute length L is sufficiently short so that this issue does not arise while also being sufficiently long so that the reported results do not depend upon L.

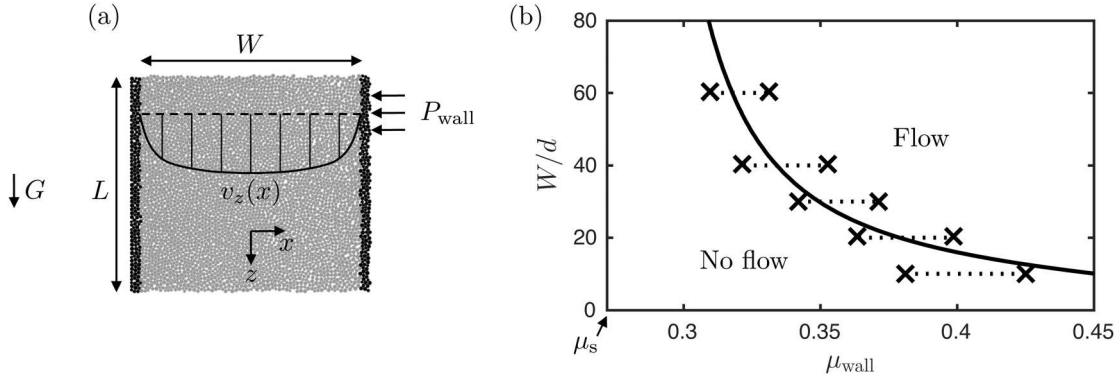

Fig. 4 (a) Configuration for two-dimensional DEM simulations of vertical chute flow for the case of W/d = 60. (b) Flow threshold locus. Symbols represent upper and lower bound estimates of the flow threshold based on the results of DEM simulations, and the solid line is the analytical flow threshold predicted by the NGF model (19).

W/d = 10, 20, 30, 40, and 60 – however, these values do vary slightly during flow – and the DEM configurations contain 633, 1270, 1900, 2539, and 3806 flowing grains, respectively.

From a quasi-static force balance, we expect the shear stress field to be $\tau(x) = |\sigma_{xz}(x)| = |\sigma_{zx}(x)| = \phi\rho_s G|x|$, where x is measured from the centerline of the chute, and the pressure field to be $P(x) = -\sigma_{xx}(x) = P_{\text{wall}}$. Again, we assume that the normal stresses are equal – *i.e.*, $\sigma_{zz} \approx \sigma_{xx}$ – and verify this assumption against the DEM results. Therefore, for vertical chute flow, the μ-field is

$$\mu(x) = \mu_{\text{wall}}\left(\frac{|x|}{W/2}\right), \tag{17}$$

where $\mu_{\text{wall}} = \phi\rho_s GW/2P_{\text{wall}}$ is the maximum value of μ, occurring at the walls ($x = \pm W/2$).

Since vertical chute flow is gravity-driven – while planar shear flow with gravity and annular shear flow are boundary-driven – our process for determining the flow threshold from DEM simulations is different than previously described. In boundary-driven flow, we specify arbitrarily-low wall velocities and extract the flow threshold from the steady-state plateau forces applied to the wall. In contrast, for gravity-driven flow, we consider various conditions – namely, combinations of W/d and μ_{wall} – and determine whether steady flow may be sustained, and in this way, the flow threshold is bounded. Our process is as follows. Motivated by the methodology of Weinhart *et al.*[10] for assessing flow arrest in DEM simulations of inclined plane flow, we utilize a criteria based on the kinetic energy. First, for a given chute width W/d, a sufficiently large value of μ_{wall} is applied so that steady flow is attained. Next, μ_{wall} is decreased to a target value – in practice, this is achieved by decreasing the acceleration of gravity G – and the system is allowed to reach steady state over a time period of $19\,470\sqrt{m/P_{\text{wall}}}$. We confirm that the μ-fields measured from steady-state DEM data are consistent with the intended μ-fields (17). Then, the mean kinetic energy per flowing grain as a function of time – denoted as $E_{\text{kin}}(t)$ – is extracted from 5000 system snapshots distributed evenly over an additional time period of $19\,470\sqrt{m/P_{\text{wall}}}$ after reaching steady state. For values of μ_{wall} in which the arithmetic average of the kinetic energy $\langle E_{\text{kin}}(t)\rangle$ is greater than $10^{-2}P_{\text{wall}}d^2$,†† flow is continuous, and $E_{\text{kin}}(t)$ is nearly time-independent with fluctuations – defined as $(\langle(E_{\text{kin}}(t) - \langle E_{\text{kin}}(t)\rangle)^2\rangle)^{1/2}$ – smaller than $\langle E_{\text{kin}}(t)\rangle$. When μ_{wall} is decreased to a value for which $\langle E_{\text{kin}}(t)\rangle = 10^{-2}P_{\text{wall}}d^2$, fluctuations increase to be roughly equal to $\langle E_{\text{kin}}(t)\rangle$, and accordingly, we identify this condition and the corresponding value of μ_{wall} as the upper bound of the flow threshold for a given W/d. As μ_{wall} is further decreased, flow becomes intermittent, and kinetic energy fluctuations further increase. In this intermittent regime, it is important to acknowledge the effect that the wall damping parameter g_p has on flow. If g_p is too low $\left(g_p/\sqrt{mk_n} \lesssim 1\right)$, wall motion is underdamped, and the associated wall oscillations prevent flow from ceasing, even when μ_{wall} is arbitrarily small. If g_p is too high $\left(g_p/\sqrt{mk_n} \gtrsim 10^4\right)$, wall motion is overdamped, and the target wall pressure P_{wall} is not achieved. We find that for our choice of $g_p/\sqrt{mk_n} = 100$, static states may be achieved while maintaining the target wall pressure. That said, using this value of g_p, at low values of μ_{wall}, wall motion can still induce isolated, infrequent grain rearrangements that are not associated with steady flow but do contribute to the kinetic energy. To remove this effect, we median filter the measured kinetic energy data $E_{\text{kin}}(t)$ for values of μ_{wall} in the intermittent regime prior to arithmetically averaging the kinetic energy data over time. When the average value of the filtered kinetic energy data decreases to a very low value of $10^{-7}P_{\text{wall}}d^2$ we deem flow to have ceased and denote the corresponding value of μ_{wall} as the lower bound of the flow threshold.

Once upper and lower bounds of the flow threshold have been determined, we may construct a phase diagram of flowing and non-flowing states for vertical chute flow, which is shown in Fig. 4(b). For a given W/d, the $\times$-symbols denote the upper and lower bounds determined as described in the preceding paragraph, and the range of μ_{wall} between the symbols corresponds to the intermediate regime of intermittent flow and is denoted by a dotted line. While the exact value of the chute

†† Since $k_n = 10^4 P_{\text{wall}}$ in our simulations, the normalization factor $P_{\text{wall}}d^2$ is related to the elastic potential energy scale, as in Weinhart *et al.*[10]

width varies in our simulations, we find that the differences between actual values of W near the flow threshold and the corresponding nominal values are less than one grain diameter in all cases, so the values of W/d appearing in Fig. 4(b) correspond to the nominal values. Due to the presence of the intermittent regime, our determination of the flow threshold in vertical chute flow is less precise than for the flow configurations considered in Sections 4.1 and 4.2; however, the increase of the measured flow threshold with decreasing system size remains clear.

To calculate the theoretical flow threshold locus predicted by the NGF model for vertical chute flow, we substitute the μ-field (17) into (6) to obtain

$$\frac{\mathrm{d}^2 g}{\mathrm{d}\tilde{x}^2} - \tilde{x} g = 0 \quad \text{where} \quad \tilde{x} = \frac{\lambda + \mu_s - \mu_{wall} x/(W/2)}{(2Ad\mu_{wall}/W)^{2/3}} \tag{18}$$

is a dimensionless transformed coordinate. The solution of (18) is $g = C_1 \mathrm{Ai}(\tilde{x}) + C_2 \mathrm{Bi}(\tilde{x})$, where $\mathrm{Ai}(\tilde{x})$ and $\mathrm{Bi}(\tilde{x})$ are the Airy functions of the first and second kind, and C_1 and C_2 are constants. The homogeneous boundary conditions consist of the symmetry condition at $x = 0$, $\mathrm{d}g/\mathrm{d}x|_{x=0} = 0$, and a homogeneous Neumann condition at the wall, $\mathrm{d}g/\mathrm{d}x|_{x=W/2} = 0$. Enforcing the boundary conditions and setting $\lambda = 0$ yields the size-dependent flow threshold for vertical chute flow:

$$\mathrm{Ai}'\left(\frac{\mu_s}{(2Ad\mu_{wall}/W)^{2/3}}\right)\mathrm{Bi}'\left(\frac{\mu_s - \mu_{wall}}{(2Ad\mu_{wall}/W)^{2/3}}\right) - \mathrm{Bi}'\left(\frac{\mu_s}{(2Ad\mu_{wall}/W)^{2/3}}\right)\mathrm{Ai}'\left(\frac{\mu_s - \mu_{wall}}{(2Ad\mu_{wall}/W)^{2/3}}\right) = 0. \tag{19}$$

For a given value of the dimensionless chute width W/d and the material parameters μ_s and A, the smallest, positive value of μ_{wall} that satisfies (19) gives the flow threshold. The theoretical flow threshold locus (19) is plotted as a solid line in Fig. 4(b), using the same material parameters μ_s and A as in Sections 4.1 and 4.2. The theoretical flow threshold locus does a reasonably good job of quantitatively capturing the DEM data for vertical chute flow.

5 Concluding remarks

In this paper, we have studied the size-dependence of the flow threshold in three different dense granular flow configurations – (1) planar shear flow with gravity, (2) annular shear flow, and (3) vertical chute flow. Importantly, the flow threshold measured in DEM simulations shows substantial size-dependence across all configurations – the details of which are affected by the form of the stress field. We have also applied the NGF model to all three flow configurations to obtain predictions of both the flow threshold and steady flow fields. Notably, we have obtained analytical solutions for the predicted size-dependent flow threshold in all three cases. The theory – using a single set of material parameters – predicts size-dependent flow thresholds that match DEM data rather well in all cases. Further, the theory simultaneously predicts steady flow fields that are quantitatively consistent with corresponding DEM data.

For illustrative purposes, a comparison of the analytical flow thresholds predicted by the NGF model for all four flow configurations discussed in this paper – inclined plane flow (8), planar shear flow with gravity (12), annular shear flow (16), and vertical chute flow (19) – is plotted in Fig. 5 with the appropriate length-scale on the vertical axis and the maximum value of μ associated with the flow configuration on the horizontal axis. Notably, size-dependent strengthening in all three configurations considered in Section 4 is significantly greater than the strengthening predicted for inclined plane flow. Recall that the strengthening predicted by the theoretical flow threshold for inclined plane flow is entirely due to boundary effects, since the μ-field is spatially constant, while the additional strengthening associated with the other three theoretical flow thresholds is due to the spatial-dependence of the stress field, rather than boundary effects. This observation illustrates that the precise nature of the μ-field has a crucial effect on the resulting flow threshold and must be accounted for when considering other size-sensitive flow stoppage phenomena.

As a final comment, providing physical justification for fluidity boundary conditions at walls remains an open issue. In the present work, our choice of a homogeneous Neumann condition was based on pragmatic grounds – since a homogeneous Dirichlet fluidity boundary condition was not directly observed in our DEM simulations – and past experience – which has shown that such a boundary condition enables an excellent description of experiments of split-bottom flow[29] and chute flow.[30] In spite of the lack of a physical underpinning for this choice, the favorable agreement between the flow thresholds measured in DEM simulations and the corresponding analytical flow thresholds predicted by the NGF model provides support for this choice of fluidity boundary condition. From a broader perspective, the issue of specifying non-standard boundary conditions arises in virtually all nonlocal constitutive approaches,[17,20,27,38] and motivating the choice of these boundary conditions from a physical perspective remains an open challenge. In the context of nonlocal fluidity models, some recent progress has been made on this point for dense emulsions,[39] and future work of this type is needed to develop a clearer microscopic understanding of granular fluidity boundary conditions.

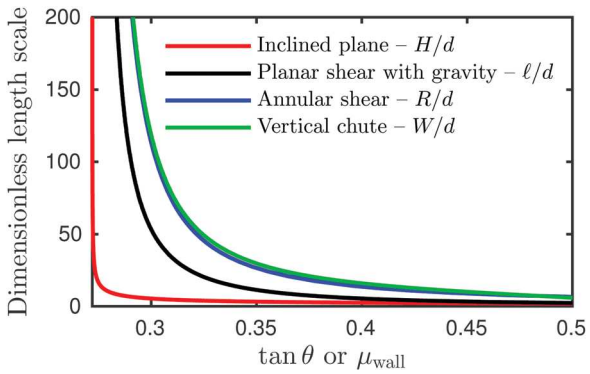

Fig. 5 Comparison of the analytical flow thresholds predicted by the NGF model for inclined plane flow (8), planar shear flow with gravity (12), annular shear flow (16), and vertical chute flow (19).

Conflicts of interest

There are no conflicts to declare.

A Averaging method

In this appendix, we briefly summarize the spatial averaging method utilized to extract steady, continuum velocity and stress fields from our DEM data. The method follows the work of Koval and coworkers[11,25] and is described for the cases of planar shear flow and planar shear flow with gravity, in which quantities are averaged over the x-coordinate shown in Fig. 1(a) and 2(a). First, for a snapshot at time t, we draw a horizontal line at a given z-position, and assign each intersected grain i a weight L_i defined as the length of the horizontal line passing through grain i. Then, with the instantaneous velocity of grain i denoted as $\mathbf{v}_i(t)$, the instantaneous velocity field is $\mathbf{v}(z,t) = \sum_i L_i \mathbf{v}_i(t) \Big/ \sum_i L_i$. Regarding the stress field, the instantaneous stress tensor associated with grain i is $\boldsymbol{\sigma}_i(t) = \left(\sum_{j \neq i} \mathbf{r}_{ij} \otimes \mathbf{f}_{ij} \right) \Big/ A_i$, where $\mathbf{r}_{ij}$ is the position vector from the center of grain i to the center of grain j, $\mathbf{f}_{ij}$ is the contact force applied on grain i by grain j, and $A_i = \pi d_i^2/4$ is the area of grain i. The instantaneous stress field follows as $\boldsymbol{\sigma}(z,t) = \sum_i L_i \boldsymbol{\sigma}_i(t)/L$, where L is the total length of the domain in the x-direction. The instantaneous velocity and stress fields are then arithmetically averaged in time over many snapshots to obtain steady fields that only depend upon the z-coordinate, such as those shown in Fig. 2(d). This process may be adapted to spatial averaging over the angular coordinate in a polar coordinate system, as described in Appendix B of Koval *et al.*,[11] and used to obtain steady fields in annular shear flow, such as those shown in Fig. 3(d).

Acknowledgements

Discussions with Ken Kamrin are gratefully acknowledged. This work was supported by funds from NSF-CBET-1552556.

References

1 G. D. R. MiDi, *Eur. Phys. J. E: Soft Matter Biol. Phys.*, 2004, **14**, 341–365.
2 F. da Cruz, S. Emam, M. Prochnow, J. Roux and F. Chevoir, *Phys. Rev. E: Stat., Nonlinear, Soft Matter Phys.*, 2005, **72**, 021309.
3 P. Jop, Y. Forterre and O. Pouliquen, *Nature*, 2006, **441**, 727–730.
4 K. Kamrin, *Int. J. Plast.*, 2010, **26**, 167–188.
5 D. C. Drucker and W. Prager, *Q. Appl. Math.*, 1952, **10**, 157–165.
6 O. Pouliquen, *Phys. Fluids*, 1999, **11**, 542–548.
7 L. E. Silbert, J. W. Landry and G. S. Grest, *Phys. Fluids*, 2003, **15**, 1–10.
8 Y. Forterre and O. Pouliquen, *J. Fluid Mech.*, 2003, **486**, 21–50.
9 T. Börzsönyi and R. E. Ecke, *Phys. Rev. E: Stat., Nonlinear, Soft Matter Phys.*, 2007, **76**, 031301.
10 T. Weinhart, A. R. Thornton, S. Luding and O. Bokhove, *Granular Matter*, 2012, **14**, 531–552.
11 G. Koval, J.-N. Roux, A. Corfdir and F. Chevoir, *Phys. Rev. E: Stat., Nonlinear, Soft Matter Phys.*, 2009, **79**, 021306.
12 Z. Tang, T. A. Brzinski, M. Shearer and K. E. Daniels, *Soft Matter*, 2018, **14**, 3040–3048.
13 D. Fenistein and M. van Hecke, *Nature*, 2003, **425**, 256.
14 T. S. Komatsu, S. Inagaki, N. Nakagawa and S. Nasuno, *Phys. Rev. Lett.*, 2001, **86**, 1757.
15 K. Nichol, A. Zanin, R. Bastien, E. Wandersman and M. van Hecke, *Phys. Rev. Lett.*, 2010, **104**, 078302.
16 O. Pouliquen and Y. Forterre, *Philos. Trans. R. Soc., A*, 2009, **367**, 5091–5107.
17 I. S. Aranson and L. S. Tsimring, *Phys. Rev. E: Stat., Nonlinear, Soft Matter Phys.*, 2002, **65**, 061303.
18 K. Kamrin and G. Koval, *Phys. Rev. Lett.*, 2012, **108**, 178301.
19 M. Bouzid, M. Trulsson, P. Claudin, E. Clément and B. Andreotti, *Phys. Rev. Lett.*, 2013, **111**, 238301.
20 K.-L. Lee and F.-L. Yang, *Phys. Rev. E*, 2017, **96**, 062909.
21 L. S. Mohan, K. K. Rao and P. R. Nott, *J. Fluid Mech.*, 2002, **457**, 377–409.
22 S. B. Savage, *J. Fluid Mech.*, 1998, **377**, 1–26.
23 J. T. Jenkins, *Phys. Fluids*, 2006, **18**, 103307.
24 K. Kamrin and D. L. Henann, *Soft Matter*, 2015, **11**, 179–185.
25 K. Kamrin and G. Koval, *Comput. Part. Mech.*, 2014, **1**, 169–176.
26 S. Plimpton, *J. Comput. Phys.*, 1995, **117**, 1–19.
27 J. Goyon, A. Colin, G. Ovarlez, A. Ajdari and L. Bocquet, *Nature*, 2008, **454**, 84–87.
28 L. Bocquet, A. Colin and A. Ajdari, *Phys. Rev. Lett.*, 2009, **103**, 036001.
29 D. L. Henann and K. Kamrin, *Proc. Natl. Acad. Sci. U. S. A.*, 2013, **110**, 6730–6735.
30 D. Liu and D. L. Henann, *J. Fluid Mech.*, 2017, **831**, 212–227.
31 D. L. Henann and K. Kamrin, *Phys. Rev. Lett.*, 2014, **113**, 178001.
32 Q. Zhang and K. Kamrin, *Phys. Rev. Lett.*, 2017, **118**, 058001.
33 A. Bhateja and D. V. Khakhar, *Rheology of dense granular flows in two dimensions: Comparison of fully two-dimensional flows to unidirectional shear flow*, 2017, arXiv:1711.01403v1.
34 D. L. Henann and K. Kamrin, *Int. J. Plast.*, 2014, **60**, 145–162.
35 P. Jop, Y. Forterre and O. Pouliquen, *J. Fluid Mech.*, 2005, **541**, 21–50.
36 J. A. Dijksman, G. H. Wortel, L. T. H. van Dellen, O. Dauchot and M. van Hecke, *Phys. Rev. Lett.*, 2011, **107**, 108303.
37 A. Ries, L. Brendel and D. E. Wolf, *Comput. Part. Mech.*, 2016, **3**, 303–310.
38 P. Chaudhuri, V. Mansard, A. Colin and L. Bocquet, *Phys. Rev. Lett.*, 2012, **109**, 036001.
39 V. Mansard, L. Bocquet and A. Colin, *Soft Matter*, 2014, **10**, 6984.